Antiferromagnetic spin fluctuations and superconductivity in NbRh$_2$B$_2$ and TaRh$_2$B$_2$ with a chiral crystal structure

Kazuaki Matano,[1] Ryo Ogura,[1] Mateo Fountaine[a],[1] Harald
O. Jeschke,[2] Shinji Kawasaki,[1] and Guo-qing Zheng[1]

[1]*Department of Physics, Okayama University, Okayama 700-8530, Japan*

[2]*Research Institute for Interdisciplinary Science,*
Okayama University, Okayama 700-8530, Japan

(Dated: October 12, 2021)

---

[a] Present address: École normale supérieure Paris-Saclay, Cachan Cedex 94235, France

1

Abstract

We report the [11]B nuclear magnetic resonance (NMR) measurements on non-centrosymmetric superconductors NbRh$_2$B$_2$ (superconducting transition temperature $T_c = 7.8$ K) and TaRh$_2$B$_2$ ($T_c = 5.9$ K) with a chiral crystal structure. The nuclear spin-lattice relaxation rate $1/T_1$ shows no coherence peak below T_c, which suggests unconventional nature of the superconductivity. In the normal state, $1/T_1T$ increases with decreasing temperature T at low temperatures below $T = 200$ K for TaRh$_2$B$_2$ and $T = 15$ K for NbRh$_2$B$_2$, while the Knight shift remains constant. These results suggest the presence of antiferromagnetic spin fluctuations in both compounds. The stronger spin fluctuations in TaRh$_2$B$_2$ compared to NbRh$_2$B$_2$ is discussed in the context of spin-orbit coupling.

I. INTRODUCTION

For a long time, the relationship between strong electronic correlations and unconventional superconductivity has been a major theme in condensed matter physics[1–3]. Antiferromagnetic spin fluctuations due to $3d$ electrons are essential for the high-temperature superconductivity in copper oxides[3, 4], and the same is true in iron pnictides[5–8] and cobalt-based superconductors[9]. In contrast, $4d$ and $5d$ electrons are usually not as strongly correlated as $3d$ electrons because of the considerably larger spatial extension of the wavefunction, while spin-orbit coupling (SOC) is stronger.

Superconductivity in compounds containing $4d$ or $5d$ elements has also attracted attention in resent years, as spin-triplet and spin-singlet mixed superconductivity has been discovered in some non-centrosymmetric superconductors (NCSs) containing $5d$ elements[10–12]. Such a mixed state is explained by the antisymmetric spin-orbit coupling (ASOC) interaction [13–15], and can show topological properties[16, 17]. Broken inversion symmetry and strong SOC also lead to the realization of Weyl semimetals[18, 19], where a huge orbital diamagnetic response has been found [20] and unconventional superconducting state has been suggested [21–23].

Among NCSs, only Li$_2$Pt$_3$B and CePt$_3$Si[24] show pronounced signature of spin-triplet properties. Li$_2$Pt$_3$B is a weakly correlated metal, but CePt$_3$Si is heavy fermion superconductor and electron correlation is strong. After Li$_2$Pt$_3$B was reported, a number of NCSs with weak electron correlations were found[25–29], but no spin-triplet superconductivity was reported[30–35]. The reason why spin-triplet superconductivity was not observed in

those compounds was probably because the ASOC was not large enough[12]. The question then, is how to enhance the ASOC. It has been found that the enhancement of the ASOC in $Li_2(Pd_{1-x}Pt_x)_3B$ is caused by the decrease in the angle between $B(Pd,Pt)_6$ octahedra, which enhances the breaking of the spatial inversion symmetry[12]. Inspection of the evolution of $Li_2(Pd_{1-x}Pt_x)_3B$ with x reveals that the local distortion in the crystal structure is another important factor in addition to the presence of the heavier element Pt[12]. Note that $Li_2(Pd,Pt)_3B$ has a chiral crystal structure, which is an advantage for achieving a large extent of symmetry breaking.

NbRh$_2$B$_2$ and TaRh$_2$B$_2$ are recently discovered superconductors ($T_c = 7.8$ K for NbRh$_2$B$_2$, 5.8 K for TaRh$_2$B$_2$) with a chiral crystal structure[36]. They have a structure with space group $P3_1$ and a large upper critical field ($H_{c2} = 18.0$ T for NbRh$_2$B$_2$, 11.7 T for TaRh$_2$B$_2$) exceeding the Pauli limit[36, 37]. It is interesting to note the similarity of the relationship between NbRh$_2$B$_2$ and TaRh$_2$B$_2$ to that between Li_2Pd_3B and Li_2Pt_3B. Like Pd and Pt, Nb and Ta are located in the same raw in the periodic table. Therefore, they provide a good platform to study the interplay between ASOC, electron correlations and superconductivity.

Here we report ^{11}B nuclear magnetic resonance (NMR) measurements of polycrystalline samples of NbRh$_2$B$_2$ and TaRh$_2$B$_2$. We find an increase of $1/T_1T$ with decreasing temperature at low temperatures for both compounds. The Knight shift is constant in the temperatures range where $1/T_1T$ is increased. These results suggest the existence of antiferromagnetic spin correlations. However, the magnitude of spin correlations is different, and it is more significant for TaRh$_2$B$_2$ where the SOC is larger. In the superconducting state, the spin-lattice relaxation rate $1/T_1$ dropped below T_c without a coherence peak witch suggests unconventional superconductivity.

II. EXPERIMENTAL AND THEORETICAL

A. Sample preparation and characterization

The polycrystalline samples of NbRh$_2$B$_2$ and TaRh$_2$B$_2$ were synthesized by heating a mixture of Nb(Ta), Rh and B in a vacuum. The elemental Nb (99.99%), Ta (99.9%), Rh (99.9%), and B (99%) were used. Powders of the starting materials Ta/Nb, Rh, and B were weighed in a ratio of 1:1.9:2.1, crushed using a mortar and pestle, and pressed into a pellet.

The pellets were wrapped in Ta foil and heated at 1200 °C for 6 h while vacuuming in a quartz tube with the order of 10^{-1} Pa. The pellets were crushed into powder for X-ray and NMR measurements. The T_c was determined by measuring the ac susceptibility using the *in situ* NMR coil. Dc susceptibility measurements were performed using a superconducting quantum interference device (SQUID) with the vibrating sample magnetometer (VSM).

B.   NMR measurements

A standard phase-coherent pulsed NMR spectrometer was used to collect data. The NMR measurements were performed at an applied magnetic field $H_0 = 3.0378$ T. The nuclear gyromagnetic ratio $\gamma=13.66$ MHz/T was used for calculation of the Knight shift. The nuclear spin-lattice relaxation rate $1/T_1T$ was measured by using a single saturation pulse. The spin-lattice relaxation time T_1 was measured by using a single saturating pulse. The recovery curves of the nuclear magnetization in all temperature ranges were fitted by a single stretched exponential function

$$\frac{M_0 - M(t)}{M_0} = 0.9e^{\left(-\frac{6t}{T_1}\right)^{\beta}} + 0.1e^{\left(-\frac{t}{T_1}\right)^{\beta}} \tag{1}$$

to extract $1/T_1$, where M_0 is the nuclear magnetization in the thermal equilibrium, $M(t)$ is the nuclear magnetization at a time t after the saturating pulse, and $\beta < 1$. In this study, β is within the range of 0.6 to 0.8.

C.   Band calculations

We used density functional theory (DFT) calculations within the full potential local orbital (FPLO) basis [38]. We use the generalized gradient approximation (GGA) to the exchange correlation functional [39], and we perform fully relativistic calculations in order to include the effects of spin-orbit (SO) coupling. For $TaRh_2B_2$, we use the crystal structure given in Ref. 36. For $NbRh_2B_2$ which is isostructural to $TaRh_2B_2$, only lattice parameters are given in Ref. 36. We use GGA calculations to optimize the internal coordinates of $NbRh_2B_2$. We are confident that the DFT structure prediction works very well in these materials because application of the same relaxation to $TaRh_2B_2$ leads only to a 60 meV lower energy per formula unit and nearly unchanged atomic positions. We use $24 \times 24 \times 24$ k meshes to calculate the band structures and densities of states.

III. RESULTS AND DISCUSSION
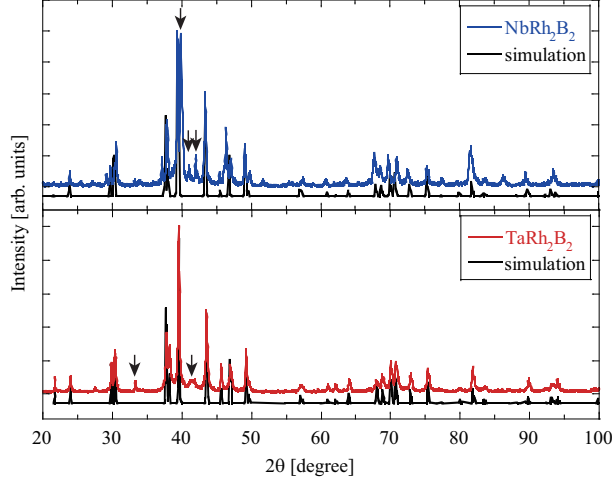
A. Spin correlations in the normal state

FIG. 1. (color online) XRD patterns for $NbRh_2B_2$ and $TaRh_2B_2$. The theoretical curves(simulations) are obtained by the Rietveld method. Arrows indicate unidentified peaks.

Figure 1 shows the powder X-ray diffraction (XRD) patterns for $NbRh_2B_2$ and $TaRh_2B_2$. The results are generally in agreement with the simulations using the Rietveld method, but impurity peaks, which have also been observed in previous studies[36], were observed in both samples. Figure 2 shows the ac susceptibility measured using the *in situ* NMR coil.
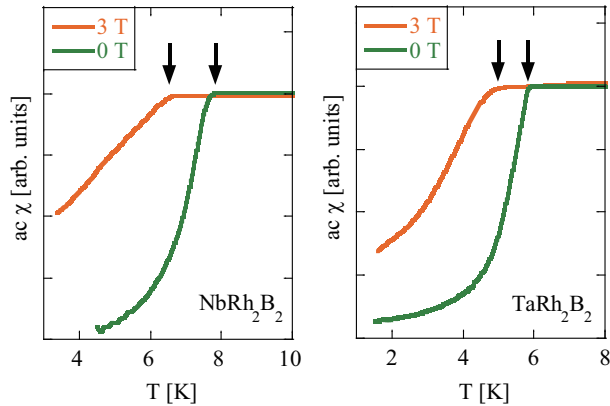

FIG. 2. (color online) Ac susceptibility measured using the *in situ* NMR coil at zero and finite magnetic field (3 T). The arrows indicate T_c for each sample at different fields.

The T_c was determined as the onset temperature of the appearance of diamagnetism. The

T_c for zero magnetic field is 7.6 K for NbRh$_2$B$_2$ and 5.8 K for TaRh$_2$B$_2$, respectively. When a magnetic field of 3 T was applied, T_c is reduced to 6.5 K for NbRh$_2$B$_2$ and 5.0 K for TaRh$_2$B$_2$, respectively. The obtained T_c is consistent with the previous report[36]. Figure 3
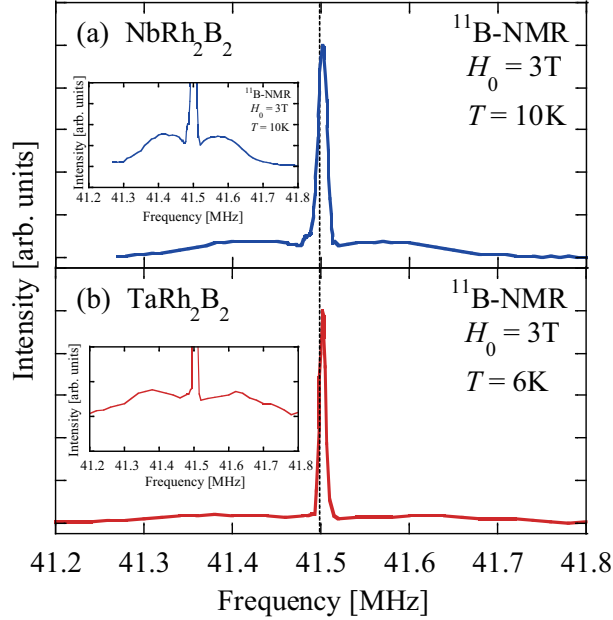

FIG. 3. (color online) (a) ^{11}B-NMR spectra at 3.0 T and 6 K for NbRh$_2$B$_2$. (b) ^{11}B-NMR spectra at 3.0 T and 10 K for TaRh$_2$B$_2$. The dotted line shows the position of K=0.

shows the ^{11}B($I = 3/2$)-NMR spectra for NbRh$_2$B$_2$ and TaRh$_2$B$_2$. A typical powder pattern is observed for both samples. The full width at the half maximum (FWHM) of the central peak is 10.2 kHz for NbRh$_2$B$_2$ and 7.4 kHz for TaRh$_2$B$_2$. Figure 4 shows the Knight shift, K, as a function of temperature. In both samples, K decreases gradually toward lower temperatures and becomes constant at 60 K. Then, with the superconducting transition, K decreased sharply with the onset of superconductivity. Figure 5 shows the temperature dependence of $1/T_1T$ for NbRh$_2$B$_2$ and TaRh$_2$B$_2$. Above 200 K, $1/T_1T$ is constant for both compounds. However, at low temperatures, $1/T_1T$ behaves differently. In TaRh$_2$B$_2$, $1/T_1T$ is greatly enhanced below 200 K, while the enhancement is weak in NbRh$_2$B$_2$.

In a general form, $1/T_1T$ is expressed as

$$\frac{1}{T_1T} = \frac{\pi k_B \gamma_n^2}{(\gamma_e \hbar)^2} \sum_q A_{hf}^2 \frac{\chi''_\perp(q,\omega)}{\omega},\tag{2}$$

where $\chi''_\perp(q,\omega)$ is the imaginary part of the dynamical susceptibility perpendicular to the applied field, and ω is the NMR frequency. If one assumes that there is a peak around a finite
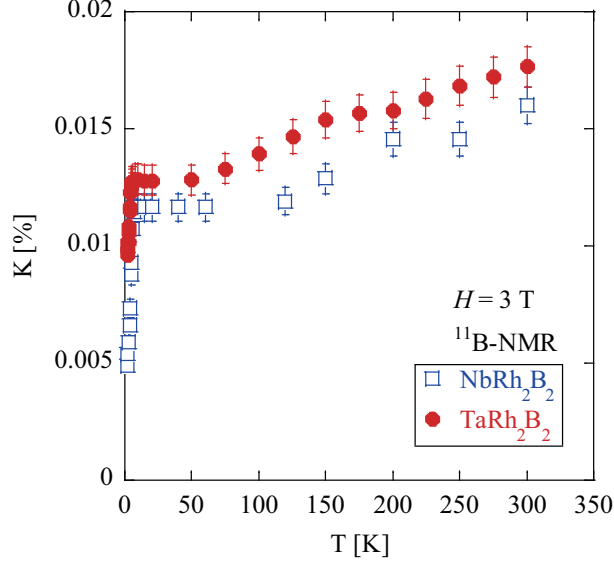
6

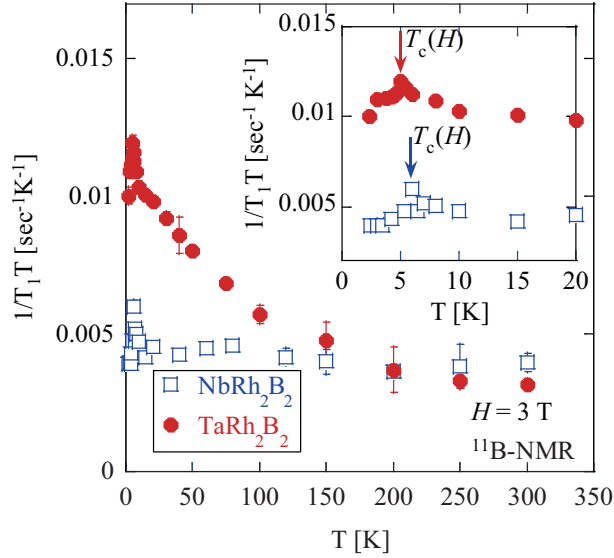FIG. 4. (color online) Temperature dependence of the Knight shift for NbRh$_2$B$_2$ and TaRh$_2$B$_2$.

FIG. 5. (color online) Temperature dependence of $1/T_1T$ measured at center peak for NbRh$_2$B$_2$ and TaRh$_2$B$_2$.

wave vector Q (due to spin fluctuation), then one may have the following approximation,

$$\frac{1}{T_1T} = \left(\frac{1}{T_1T}\right)_0 + \left(\frac{1}{T_1T}\right)_Q$$

$$\left(\frac{1}{T_1T}\right)_Q = \frac{\pi k_{\mathrm{B}}\gamma_n^2}{(\gamma_e\hbar)^2}\sum_{q\approx Q} A_{hf}^2 \frac{\chi_{\perp}''(q,\omega)}{\omega}, \tag{3}$$

where $(1/T_1T)_Q$ is the contribution from wave vectors around Q, while $(1/T_1T)_0$ denotes

the contribution from $q \sim 0$, which is proportional to the magnetic susceptibility χ_s. That is, $(1/T_1 T)_0$ is proportional to the density of states (DOS) at the Fermi level and does not change with temperature. Therefore, the increase of $1/T_1 T$ at low temperatures is ascribed to $(1/T_1 T)_Q$, due to the development of the spin correlation appears at low temperatures. On the other hand, since the temperature dependence of the Knight shift is constant above T_c in both samples, we conclude that the correlation is of antiferromagnetic in nature. The difference in the strength of the antiferromagnetic fluctuations between NbRh$_2$B$_2$ to TaRh$_2$B$_2$ will be discussed in subsection C in connection to the calculated band structure.

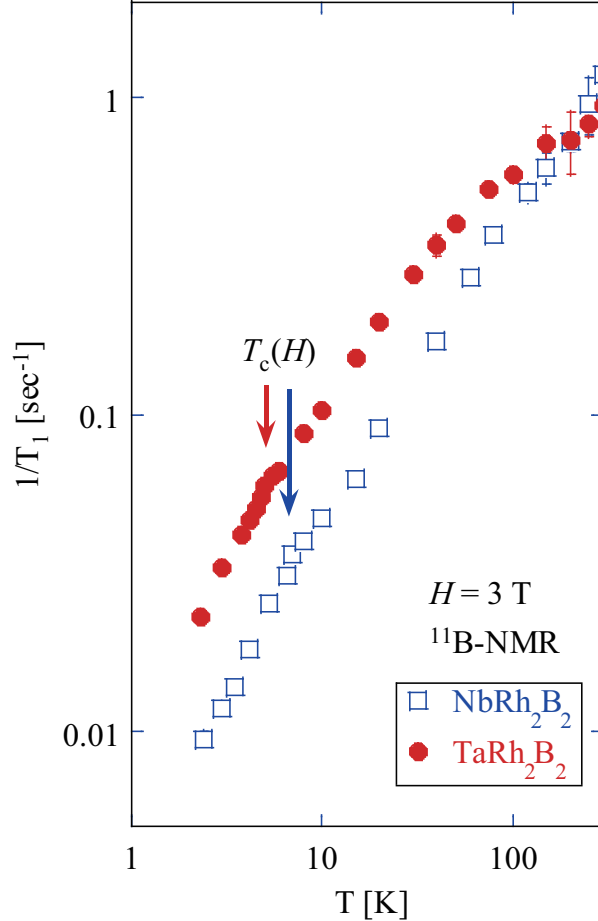## B. Properties of the superconducting state

FIG. 6. (color online) Temperature dependence of the spin-lattice relaxation rate $1/T_1$ measured at the central peak.

Figure 6 shows the temperature dependence of $1/T_1$ measured at the central peak of

the NMR spectrum at $H_0 = 3.0$ T. Below T_c, $1/T_1$ decreases due to the superconducting transition, but no clear coherence peak was observed for either compound. In BCS superconductors, a large coherence peak is usually observed. A large applied magnetic field could reduce the height of the coherence peak, but the applied magnetic field (3 T) we used is only 1/6 of the upper critical field (18 T) for $NbRh_2B_2$ and 1/4 for $TaRh_2B_2$ (11.7 T), which is not strong enough to completely suppress the coherence peak[36, 40]. Large nuclear electric quadrupole moment [41], or phonon damping in the strong coupling regime[35, 42] could result in an absence of the coherence peak. However, the former dose not apply to [11]B nuclei, and there is no indication of strong-coupling superconductivity as the decrease of $1/T_1$ below T_c is not steep. Therefore, the absence of the coherence peak may indicate the possibility of unconventional superconductivity.In the case of Li_2Pd_3B and Li_2Pt_3B, a well-defined coherence peak was found in the former[43] but no coherence peak in the latter, which was explained by the different strength of SOC. However, in the present case, no coherence peak is seen in both compounds although the SOC is quite different(see section C), which should probably be ascribed to electron correlations. The decrease of $1/T_1$ below T_c is not as fast as T^3 as seen in, for example, cuprates, which is probably due to impurity scattering[44]. In unconventional superconductors with line nodes in the gap function, impurity scattering can bring about a finite density of states. In fact, when the residual density of states is quite large, the temperature dependence of $1/T_1$ similar to our result was observed[45].

The temperature dependence of the Knight shift around T_c is shown in Fig. 7. Generally, the Knight shift in the superconducting state is expressed as,

$$K = K_{orb} + K_s + K_{dia}, \tag{4}$$

$$K_{orb} = A_{orb}\chi_{orb} = 2\chi_{orb}\left\langle\frac{1}{r^3}\right\rangle, \tag{5}$$

$$K_s = A_{hf}\chi_s, \tag{6}$$

$$\chi_s = -4\mu_B^2 \int N_S(E)\frac{\partial f(E)}{\partial E}dE, \tag{7}$$

where K_{orb} is the contribution due to orbital susceptibility which is T-independent, A_{orb} and $A_{hf}$is the hyperfine coupling constant, χ_{orb} and χ_s are the orbital and spin susceptibility, and K_{dia} is the contribution from diamagnetism in the vortex state. The K_{dia} is calculated using the following equation for the diamagnetic field H_{dia} [46],

$$H_{dia} = H_{c1}\frac{\ln\left(\frac{\beta d}{\sqrt{e}\xi}\right)}{\ln\frac{\lambda}{\xi}}. \tag{8}$$
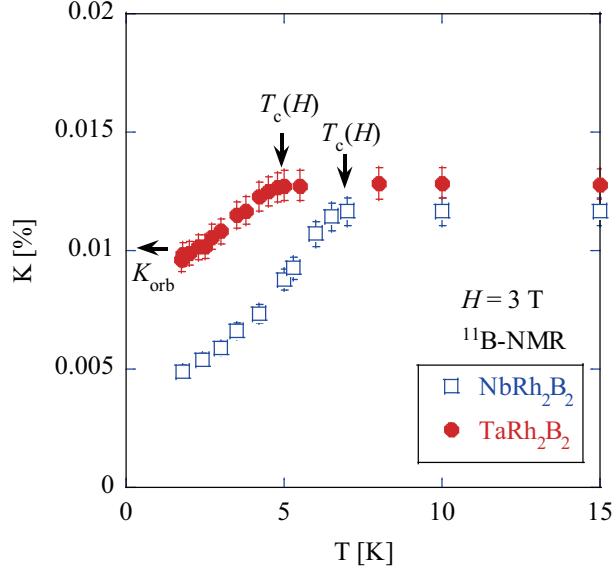
FIG. 7. (color online) Temperature dependence of the Knight shift around T_c for NbRh$_2$B$_2$ and TaRh$_2$B$_2$. The horizontal arrow indicates the position of K_{orb} (See text).

Here, β is 0.38 for the triangular lattice of the vortex, ξ is the coherence length, λ is the London penetration depth. ξ is obtained from the measurement of H_{c2} and λ is taken from Ref. 36. As a result, K_{dia} was calculated to be -0.025 % for NbRh$_2$B$_2$ and -0.015 % for TaRh$_2$B$_2$, which are larger than the observed reduction of the Knight shift below T_c.

Next, we estimate the A_{hf} and K_{orb} using the K-χ plot. In Fig. 8, the Knight shift for the TaRh$_2$B$_2$ is plotted as a function of DC susceptibility. The diamagnetic susceptibility due to closed shells of Ta, Rh, and B was estimated to be χ_{core} -1.6×10^{-6} emu/mol [47], from which the slope of $K_{\mathrm{orb}} = A_{\mathrm{orb}}\chi_{\mathrm{orb}}$ was drawn. Here, $\langle 1/r^3 \rangle$=0.62 a.u. is adopted, which is 80% of the theoretical value for B metal[48]. From K-χ plot, the hyperfine coupling constant is extracted as A_{hf}= 504 kOe/μ_{B}. The orbital part of the shift and susceptibility are $K_{\mathrm{orb}} = 0.01\%$, $\chi_{\mathrm{orb}} = -9.26 \times 10^{-6}\,\mathrm{emu\,/\,mol \cdot B}$. The Knight shift for NbRh$_2$B$_2$ is reduced below K_{orb}, thus most of the decrease can be attributed to the contribution of K_{dia}. Therefore, we cannot discuss K_{s} below T_c at the moment.

C. Band structure and other observed properties

In order to understand our results, we performed electronic structure calculations for NbRh$_2$B$_2$ and TaRh$_2$B$_2$. Figure 9 shows fully relativistic GGA bands, labeled as GGA+SO.
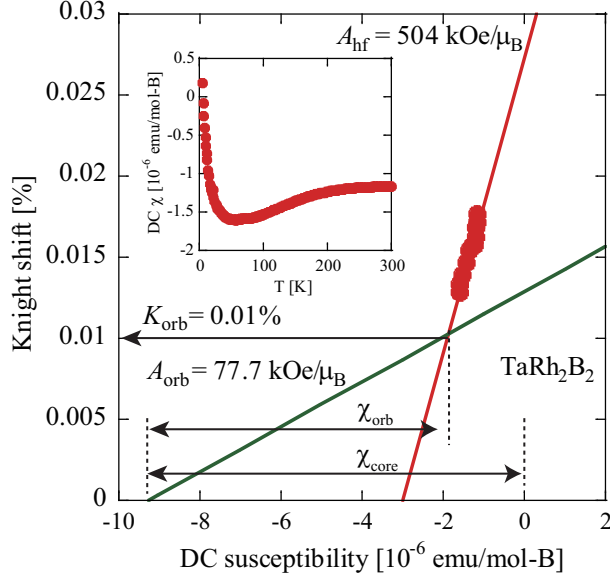
10

FIG. 8. (color online) K-χ plot for TaRh$_2$B$_2$. The inset shows the results of the dc magnetic susceptibility measurement. The Curie-Weiss-like increase in the DC susceptibility at low temperatures is probably due to paramagnetic impurities.

There is a significant splitting of bands due to spin-orbit coupling; this effect is more pronounced in TaRh$_2$B$_2$ containing heavier Ta compared to NbRh$_2$B$_2$.

We first discuss the differences in T_c between NbRh$_2$B$_2$ (7.8 K) and TaRh$_2$B$_2$ (5.9 K). We evaluated the density of states at the Fermi level N_{EF}. We found $N_{EF} = 3.04564$ states/eV/f.u. (f.u. = formula unit) for NbRh$_2$B$_2$ and $N_{EF} = 2.77660$ states/eV/f.u. for TaRh$_2$B$_2$. Such differences in DOS may be caused by differences in the magnitude of the spin-orbit interaction, namely the magnitude of the band splitting. The N_{EF} is about 9% smaller in TaRh$_2$B$_2$, explaining at least partly why the experimentally observed superconducting T_c is also smaller.

This calculation at first sight seems to contradict with the results of the Knight shift. The Knight shift of TaRh$_2$B$_2$ is larger than that of NbRh$_2$B$_2$. According to Equation (4) to (7), assuming that K_{orb} and A_{hf} are the same for NbRh$_2$B$_2$ and TaRh$_2$B$_2$, the Knight shift is proportional to the density of states. The difference of the Knight shift indicates that the density of states in TaRh$_2$B$_2$ is larger than in NbRh$_2$B$_2$. However, what we observe in ^{11}B-NMR is the contribution of the s-electrons. If we take into account only the s-electrons, N_{EF} is 0.070 states/eV/f.u. for NbRh$_2$B$_2$ and 0.076 states/eV/f.u. for TaRh$_2$B$_2$ and the contradiction is resolved.
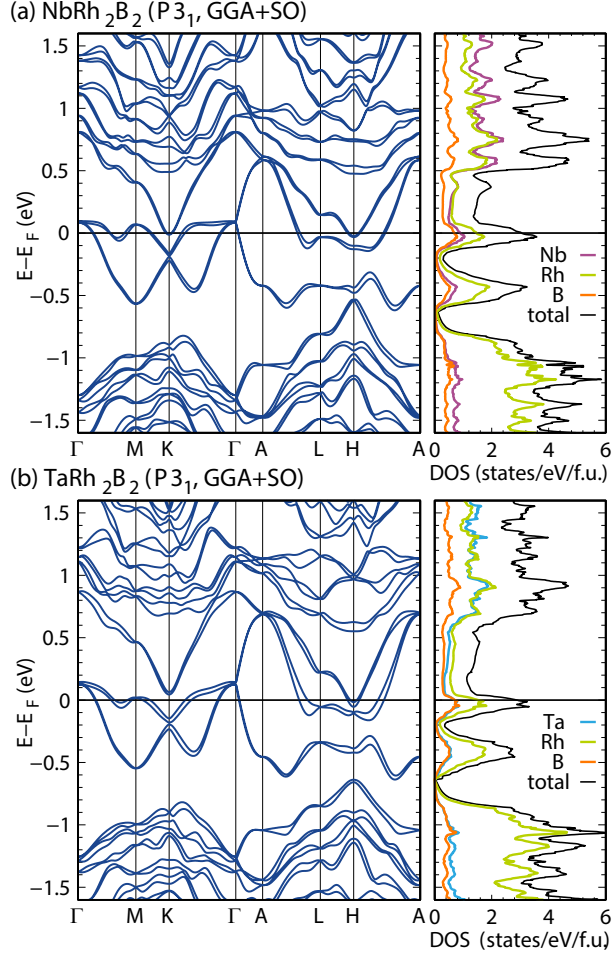
FIG. 9. (color online) Band structures and density of states of (a) $NbRh_2B_2$ and (b) $TaRh_2B_2$.

Next, we will discuss effects of the ASOC. For $Li_2(Pt,Pd)_3B$, the effect of the ASOC is discussed in terms of band splitting near the Fermi level, which is calculated to be 200 meV for Li_2Pt_3B and 30 meV for Li_2Pd_3B[49]. In Fig. 8, the band splitting near the L point is calculated to be 140 meV for $TaRh_2B_2$ and 30 meV for $NbRh_2B_2$. Spin-orbit interactions and electron correlations are usually not reciprocal in nature. Namely, in systems with strong electron correlations, SOC is weak and in systems with large SOC, electron correlations are weak. However, there are some exceptions to this principle. Contrary to the usual case, the compound Sr_2IrO_4 containing heavy element is a Mott insulator, while Sr_2CoO_4 and Sr_2RhO_4 are metals [50–53]. Spin-orbit interactions can explain this difference. Sr_2IrO_4 contains a slightly tilted IrO_6 octahedra[53]. The stranger ionic nature of the oxide leads to an approximately 5/6 filled t_{2g} shell of Ir. As a result, a Mott insulator is realized. The Mott insulator is realized when spin-orbit interactions and Coulomb interaction further split

the orbitals that were initially split by the crystal field in Sr_2IrO_4[52].

A similar SOC-assisted electron correlations may be realized in $(Nb,Ta)Rh_2B_2$, although $NbRh_2B_2$ and $TaRh_2B_2$ are intermetallic compounds. Boron tends to form covalent bonds, and since the electronegativities of B, Rh, and Ta/Nb are similar, no substantial transfer of charge is expected. The character of the partially filled bands of $NbRh_2B_2$ and $TaRh_2B_2$ still has to be worked out. Another possibility is the nesting of the Fermi surface. It can be seen that several bands are crossing the Fermi level. The spin-orbit interaction may have caused a different Fermi level nesting between the two materials. As mentioned above, the SOC is larger in $TaRh_2B_2$. We calculated the electronic structure of $NbRh_2B_2$ and $TaRh_2B_2$ using $200 \times 200\ k$ meshes and the GGA+SO functional in order to extract the Fermi surfaces at three different k_z values. The result is shown in Fig.10. The splitting of bands due to SOC is clearly stronger in $TaRh_2B_2$, and the Fermi surface nesting is quite different for the two compounds. For example, the six-fold symmetric Fermi surface for $TaRh_2B_2$ appears to have a better nesting condition compared to $NbRh_2B_2$.
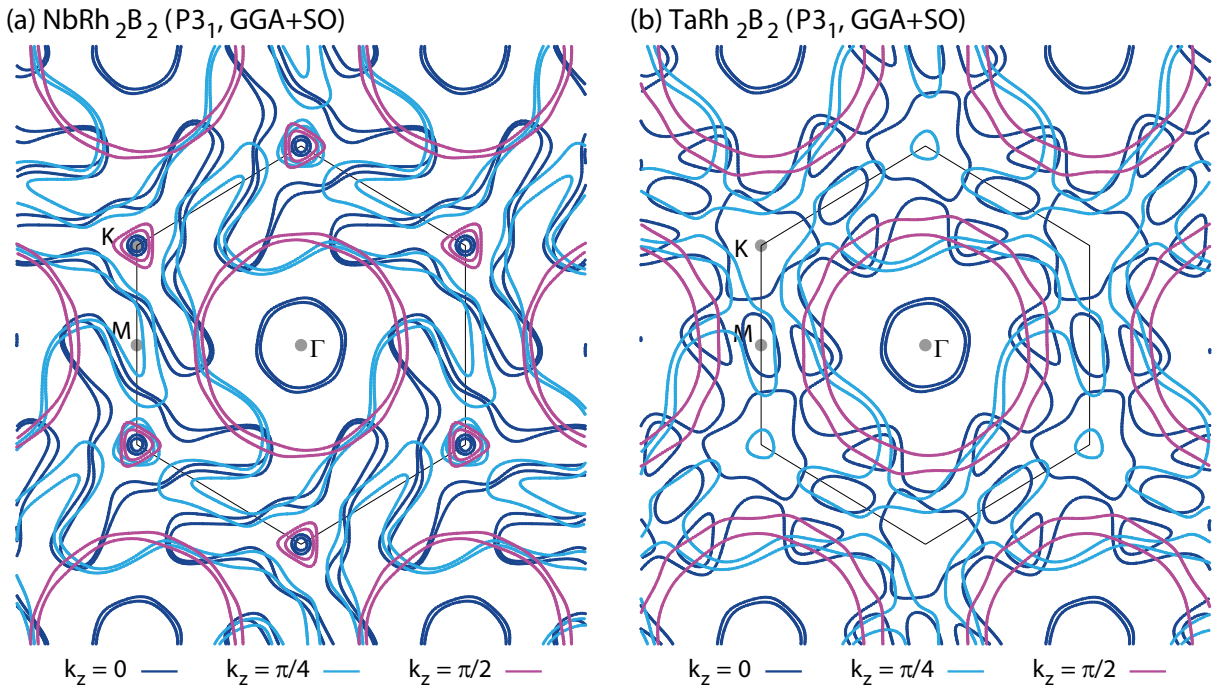

FIG. 10. GGA+SO Fermi surface cuts of (a) $NbRh_2B_2$ and (b) $TaRh_2B_2$. The Brillouin zone and high symmetry points at $k_z = 0$ are shown.

IV. SUMMARY

In summary, we have performed ^{11}B-NMR measurements on the non-centrosymmetric superconductors NbRh$_2$B$_2$ and TaRh$_2$B$_2$ with chiral structure. In both compounds, we found that $1/T_1T$ increases with decreasing T at low temperatures. On the other hand, the Knight shift was constant at low temperatures for both compounds. These results point to the existence of antiferromagnetic spin correlations. Furthermore, the magnitude of the spin correlation is much more significant for TaRh$_2$B$_2$ than NbRh$_2$B$_2$. It is not usual for compounds containing heavy elements to have stronger spin correlations. It is necessary to consider the possibility that spin-orbit interactions enhance spin correlations in this system. We hope that our result will stimulate more works in this direction. In the superconducting state, no coherence peak was observed in $1/T_1$ just below T_c, suggesting unconventional superconductivity.

---

[1] P. A. Lee, N. Nagaosa, and X.-G. Wen, Doping a Mott insulator: Physics of high-temperature superconductivity, Rev. Mod. Phys. **78**, 17 (2006).

[2] T. Moriya and K. Ueda, Spin fluctuations and high temperature superconductivity, Adv. Phys. **49**, 555 (2000).

[3] P. Monthoux and D. Pines, Spin-fluctuation-induced superconductivity and normal-state properties of YBa$_2$Cu$_3$O$_7$, Phys. Rev. B **49**, 4261 (1994).

[4] S. Ohsugi, Y. Kitaoka, K. Ishida, G.-q. Zheng, and K. Asayama, Cu NMR and NQR Studies of High-T_c Superconductor La$_{2-x}$Sr$_x$CuO$_4$, J. Phys. Soc. Jpn. **63**, 700 (1994).

[5] I. I. Mazin, D. J. Singh, M. D. Johannes, and M. H. Du, Unconventional Superconductivity with a Sign Reversal in the Order Parameter of LaFeAsO$_{1-x}$F$_x$, Phys. Rev. Lett. **101**, 057003 (2008).

[6] K. Kuroki, S. Onari, R. Arita, H. Usui, Y. Tanaka, H. Kontani, and H. Aoki, Unconventional Pairing Originating from the Disconnected Fermi Surfaces of Superconducting $LaFeAsO_{1-x}F_x$, Phys. Rev. Lett. **101**, 087004 (2008).

[7] K. Matano, Z. Li, G. L. Sun, D. L. Sun, C. T. Lin, M. Ichioka, and G. qing Zheng, Anisotropic spin fluctuations and multiple superconducting gaps in hole-doped $Ba_{0.72}K_{0.28}Fe_2As_2$: NMR in a single crystal, Europhys. Lett. **87**, 27012 (2009).

[8] T. Oka, Z. Li, S. Kawasaki, G. F. Chen, N. L. Wang, and G.-q. Zheng, Antiferromagnetic Spin Fluctuations above the Dome-Shaped and Full-Gap Superconducting States of $LaFeAsO_{1-x}\mathbf{F}_x$ Revealed by ^{75}As-Nuclear Quadrupole Resonance, Phys. Rev. Lett. **108**, 047001 (2012).

[9] K. Matano, C. T. Lin, and G. qing Zheng, Hydration-induced anisotropic spin fluctuations in $Na_xCoO_2 \cdot 1.3H_2O$ superconductor, Europhys. Lett. **84**, 57010 (2008).

[10] M. Nishiyama, Y. Inada, and G.-q. Zheng, Spin Triplet Superconducting State due to Broken Inversion Symmetry in Li_2Pt_3B, Phys. Rev. Lett. **98**, 047002 (2007).

[11] H. Q. Yuan, D. F. Agterberg, N. Hayashi, P. Badica, D. Vandervelde, K. Togano, M. Sigrist, and M. B. Salamon, S-Wave Spin-Triplet Order in Superconductors without Inversion Symmetry: Li_2Pd_3B and Li_2Pt_3B, Phys. Rev. Lett. **97**, 017006 (2006).

[12] S. Harada, J. J. Zhou, Y. G. Yao, Y. Inada, and G.-q. Zheng, Phys. Rev. B **86**, 220502(R) (2012).

[13] L. P. Gor'kov and E. I. Rashba, Superconducting 2D System with Lifted Spin Degeneracy: Mixed Singlet-Triplet State, Phys. Rev. Lett. **87**, 037004 (2001).

[14] P. A. Frigeri, D. F. Agterberg, A. Koga, and M. Sigrist, Superconductivity without Inversion Symmetry: MnSi versus $CePt_3Si$, Phys. Rev. Lett. **92**, 097001 (2004).

[15] P. A. Frigeri, D. F. Agterberg, and M. Sigrist, Spin susceptibility in superconductors without inversion symmetry, New J. Phys. **6**, 115 (2004).

[16] M. Sato and S. Fujimoto, Topological phases of noncentrosymmetric superconductors: Edge states, Majorana fermions, and non-Abelian statistics, Phys. Rev. B **79**, 094504 (2009).

[17] Y. Tanaka, Y. Mizuno, T. Yokoyama, K. Yada, and M. Sato, Anomalous Andreev Bound State in Noncentrosymmetric Superconductors, Phys. Rev. Lett. **105**, 097002 (2010).

[18] H. Weng, C. Fang, Z. Fang, B. A. Bernevig, and X. Dai, Weyl Semimetal Phase in Noncentrosymmetric Transition-Metal Monophosphides, Phys. Rev. X **5**, 011029 (2015).

[19] L. X. Yang, Z. K. Liu, Y. Sun, H. Peng, H. F. Yang, T. Zhang, B. Zhou, Y. Zhang, Y. F. Guo, M. Rahn, D. Prabhakaran, Z. Hussain, S.-K. Mo, C. Felser, B. Yan, and Y. L. Chen, Weyl semimetal phase in the non-centrosymmetric compound TaAs, Nat. Phys. **11**, 728 (2015).

[20] C. G. Wang, Y. Honjo, L. X. Zhao, G. F. Chen, K. Matano, R. Zhou, and G.-q. Zheng, Landau diamagnetism and Weyl-fermion excitations in TaAs revealed by ^{75}As NMR and NQR, Phys. Rev. B **101**, 241110(R) (2020).

[21] T. Meng and L. Balents, Weyl superconductors, Phys. Rev. B **86**, 054504 (2012).

[22] G. Y. Cho, J. H. Bardarson, Y.-M. Lu, and J. E. Moore, Superconductivity of doped Weyl semimetals: Finite-momentum pairing and electronic analog of the ^{3}He-A phase, Phys. Rev. B **86**, 214514 (2012).

[23] Y. Qi, P. G. Naumov, M. N. Ali, C. R. Rajamathi, W. Schnelle, O. Barkalov, M. Hanfland, S.-C. Wu, C. Shekhar, Y. Sun, V. Süß, M. Schmidt, U. Schwarz, E. Pippel, P. Werner, R. Hillebrand, T. Förster, E. Kampert, S. Parkin, R. J. Cava, C. Felser, B. Yan, and S. A. Medvedev, Superconductivity in Weyl semimetal candidate MoTe2, Nature Communications **7**, 11038 (2016).

[24] H. Mukuda, T. Fujii, T. Ohara, A. Harada, M. Yashima, Y. Kitaoka, Y. Okuda, R. Settai, and Y. Onuki, Enhancement of Superconducting Transition Temperature due to the Strong Antiferromagnetic Spin Fluctuations in the Noncentrosymmetric Heavy-Fermion Superconductor CeIrSi$_3$: A ^{29}Si NMR Study under Pressure, Phys. Rev. Lett. **100**, 107003 (2008).

[25] T. Klimczuk, Q. Xu, E. Morosan, J. D. Thompson, H. W. Zandbergen, and R. J. Cava, Superconductivity in noncentrosymmetric Mg$_{10}$Ir$_{19}$B$_{16}$, Phys. Rev. B **74**, 220502(R) (2006).

[26] A. Kawano, Y. Mizuta, H. Takagiwa, T. Muranaka, and J. Akimitsu, The Superconductivity in Re-B System, Journal of the Physical Society of Japan **72**, 1724 (2003).

[27] G. Goll, M. Marz, A. Hamann, T. Tomanic, K. Grube, T. Yoshino, and T. Takabatake, Thermodynamic and transport properties of the non-centrosymmetric superconductor LaBiPt, Physica B: Condensed Matter **403**, 1065 (2008).

[28] B. Joshi, A. Thamizhavel, and S. Ramakrishnan, Superconductivity in noncentrosymmetric BiPd, Phys. Rev. B **84**, 064518 (2011).

[29] M. N. Ali, Q. D. Gibson, T. Klimczuk, and R. J. Cava, Noncentrosymmetric superconductor with a bulk three-dimensional Dirac cone gapped by strong spin-orbit coupling, Phys. Rev. B **89**, 020505(R) (2014).

[30] K. Tahara, Z. Li, H. X. Yang, J. L. Luo, S. Kawasaki, and G.-q. Zheng, Superconducting state in the noncentrosymmetric $Mg_{9.3}Ir_{19}B_{16.7}$ and $Mg_{10.5}Ir_{19}B_{17.1}$ revealed by NMR, Phys. Rev. B **80**, 060503(R) (2009).

[31] E. Bauer, G. Rogl, X.-Q. Chen, R. T. Khan, H. Michor, G. Hilscher, E. Royanian, K. Kumagai, D. Z. Li, Y. Y. Li, R. Podloucky, and P. Rogl, Unconventional superconducting phase in the weakly correlated noncentrosymmetric Mo_3Al_2C compound, Phys. Rev. B **82**, 064511 (2010).

[32] K. Matano, S. Maeda, H. Sawaoka, Y. Muro, T. Takabatake, B. Joshi, S. Ramakrishnan, K. Kawashima, J. Akimitsu, and G.-q. Zheng, NMR and NQR Studies on Non-centrosymmetric Superconductors Re_7B_3, LaBiPt, and BiPd, J. Phys. Soc. Jpn. **82**, 084711 (2013).

[33] Singh, R. P. and Hillier, A. D. and Mazidian, B. and Quintanilla, J. and Annett, J. F. and Paul, D. McK. and Balakrishnan, G. and Lees, M. R., Detection of Time-Reversal Symmetry Breaking in the Noncentrosymmetric Superconductor Re_6Zr Using Muon-Spin Spectroscopy, Phys. Rev. Lett. **112**, 107002 (2014).

[34] K. Matano, R. Yatagai, S. Maeda, and G.-q. Zheng, Full-gap superconductivity in noncentrosymmetric $Re_6Zr, Re_{27}Zr_5$, and $Re_{24}Zr_5$, Phys. Rev. B **94**, 214513 (2016).

[35] S. Maeda, K. Matano, and G.-q. Zheng, Fully gapped spin-singlet superconductivity in noncentrosymmetric $PbTaSe_2$: ^{207}Pb nuclear magnetic resonance study, Phys. Rev. B **97**, 184510 (2018).

[36] E. M. Carnicom, W. Xie, T. Klimczuk, J. Lin, K. Górnicka, Z. Sobczak, N. P. Ong, and R. J. Cava, $TaRh_2B_2$ and $NbRh_2B_2$: Superconductors with a chiral noncentrosymmetric crystal structure, Sci. Adv. **4**, eaar7969 (2018).

[37] D. A. Mayoh, M. J. Pearce, K. Götze, A. D. Hillier, G. Balakrishnan, and M. R. Lees, Superconductivity and the upper critical field in the chiral noncentrosymmetric superconductor $NbRh_2B_2$, Journal of Physics: Condensed Matter **31**, 465601 (2019).

[38] K. Koepernik and H. Eschrig, Full-potential nonorthogonal local-orbital minimum-basis band-structure scheme, Phys. Rev. B **59**, 1743 (1999).

[39] J. P. Perdew, K. Burke, and M. Ernzerhof, Generalized Gradient Approximation Made Simple, Phys. Rev. Lett. **77**, 3865 (1996).

[40] Y. Masuda and N. Okubo, Nuclear Spin-Lattice Relaxation in Superconducting Mixed State, J. Phys. Soc. Jpn. **26**, 309 (1969).

[41] Z. Li, W. H. Jiao, G. H. Cao, and G.-q. Zheng, Charge fluctuations and nodeless super-conductivity in quasi-one-dimensional $Ta_4Pd_3Te_{16}$ revealed by ^{125}Te-NMR and ^{181}Ta-NQR, Phys. Rev. B **94**, 174511 (2016).

[42] J. Luo, J. Yang, S. Maeda, Z. Li, and G.-Q. Zheng, Structural phase transition, pre-cursory electronic anomaly, and strong-coupling superconductivity in quasi-skutterudite $(Sr_{1-x}Ca_x)_3Ir_4Sn_{13}$ and $Ca_3Rh_4Sn_{13}$, Chin. Phys. **27**, 077401 (2018).

[43] M. Nishiyama, Y. Inada, and G.-q. Zheng, Superconductivity of the ternary boride Li_2Pd_3B probed by ^{11}B NMR, Phys. Rev. B **71**, 220505(R) (2005).

[44] K. Asayama, G.-q. Zheng, Y. Kitaoka, K. Ishida, and K. Fujiwara, NMR study of high-T_c superconductors , Physica C **178**, 281 (1991).

[45] S. Kawasaki, T. Oka, A. Sorime, Y. Kogame, K. Uemoto, K. Matano, J. Guo, S. Cai, L. Sun, J. L. Sarrao, J. D. Thompson, and G.-q. Zheng, Localized-to-itinerant transition preceding antiferromagnetic quantum critical point and gapless superconductivity in cerh0.5ir0.5in5, Communications Physics **3**, 148 (2020).

[46] P. G. de Gennes, *Superconductivity of Metals and Alloys* (Westview Press, Oxford, UK, 1999).

[47] G. C. Carter, L. H. Bennett, and D. J. Kahan, Metallic Shifts in NMR: A Review of the Theory and Comprehensive Critical Data Compilation of Metallic Materials (Progress in Materials Science Vol 20), Physics Bulletin **28**, 521 (1977).

[48] R. Ahlberg, Handbook of atomic data. S. Fraga, I. Karwowski, and K. M. S. Sexena. Elsevier Scientific Publishing Company, Amsterdam, Oxford, New York, Int. J. Quant. Chem. **12**, 231 (1977).

[49] K.-W. Lee and W. E. Pickett, Crystal symmetry, electron-phonon coupling, and supercon-ducting tendencies in Li_2Pd_3B and Li_2Pt_3B, Phys. Rev. B **72**, 174505 (2005).

[50] J. Matsuno, Y. Okimoto, Z. Fang, X. Z. Yu, Y. Matsui, N. Nagaosa, M. Kawasaki, and Y. Tokura, Metallic Ferromagnet with Square-Lattice CoO_2 Sheets, Phys. Rev. Lett. **93**, 167202 (2004).

[51] B. J. Kim, J. Yu, H. Koh, I. Nagai, S. I. Ikeda, S.-J. Oh, and C. Kim, Missing xy-Band Fermi Surface in $4d$ Transition-Metal Oxide Sr_2RhO_4: Effect of the Octahedra Rotation on the Electronic Structure, Phys. Rev. Lett. **97**, 106401 (2006).

[52] B. J. Kim, H. Jin, S. J. Moon, J.-Y. Kim, B.-G. Park, C. S. Leem, J. Yu, T. W. Noh, C. Kim, S.-J. Oh, J.-H. Park, V. Durairaj, G. Cao, and E. Rotenberg, Novel $J_{\text{eff}} = 1/2$ Mott State

Induced by Relativistic Spin-Orbit Coupling in Sr_2IrO_4, Phys. Rev. Lett. **101**, 076402 (2008).

[53] H. Watanabe, T. Shirakawa, and S. Yunoki, Microscopic Study of a Spin-Orbit-Induced Mott Insulator in Ir Oxides, Phys. Rev. Lett. **105**, 216410 (2010).